UNIVERSITY of CALIFORNIA

SANTA CRUZ

EVOLUTION OF BLISTER-TYPE HII REGIONS IN A MAGNETIZED MEDIUM

A thesis submitted in partial satisfaction of the
requirements for the degree of

BACHELOR OF SCIENCE

in

ASTROPHYSICS

by

Leo Gendelev

8 June 2011

The thesis of Leo Gendelev is approved by:

_____   _____
Professor Mark Krumholz   Professor Adriane Steinacker
Advisor   Theses Coordinator

_____
Professor David P. Belanger
Chair, Department of Physics

Abstract

Evolution of Blister-Type HII Regions in a Magnetized Medium

by

Leo Gendelev

We use the three-dimensional Athena ionizing radiation-magnetohydrodynamics (IRMHD) code to simulate blister-type HII regions driven by stars on the edge of magnetized gas clouds. We compare these to simulations of spherical HII regions where the star is embedded deep within a cloud, and to non-magnetized simulations of both types, in order to compare their ability to drive turbulence and influence star formation. We find that magnetized blister HII regions are very efficient at injecting energy into clouds. This is partly a magnetic effect: the magnetic energy added to a cloud by an HII region is comparable to or larger than the kinetic energy, and magnetic fields can also help collimate the ejected gas, increasing its energy yield. As a result of these effects, a blister HII region expanding into a cloud with a magnetic field perpendicular to its edge injects twice as much energy by 5 Myr as a non-magnetized blister HII region driven by a star of the same luminosity. Blister HII regions are also more efficient at injecting energy than spherical HII regions, due to the recoil provided by escaping gas, but not by as much as predicted by some analytic approximations.

Contents

Acknowledgements

I would like to thank my advisor, Professor Mark Krumholz, for all the time and effort he has spent in guiding me through this project, and for bearing with me through the difficulties I had in debugging the complex Athena code. Without him I would certainly not have been able to work on a topic within Astrophysics that was so interesting and appealing to me. I would also like to thank my two most wonderful parents, best friends, and mentors in the world, without whom I would not have had the drive or emotional support to take on such a project.

1

Introduction

Molecular Gas Clouds (MGCs) were first discovered not by their beautiful complexity but by their dark simplicity. In 1774, Sir William Herschel noticed a dark void in space and famously proclaimed, "Truly there must be a hole in the sky!" This marked the discovery of MGCs. Eventually, with the advent of infrared and radio telescopes, the true nature of these MGCs became evident. They were not voids in space but vast clouds of interstellar dust and gas, absorbing light from the stars behind them. Thousands of these clouds, predominately situated in the spiral arms of the Milky Way, have been discovered to date - collapsing under their own weight to form stars. The study of MGCs continues to be an active area of research in astrophysics because the detailed physics governing them is poorly understood.

MGCs evolve over a time scale of millions of years, so the only observational data we can obtain are snapshots of how MGCs look at certain points in their evolution. This is further complicated by the difficulties involved in observing the fine structure of MGCs, which is why computer simulations are crucial in helping us in the construction

of complete and accurate physical models of the evolution of MGCs and star formation. We can test a simple model against the result of a high resolution simulation by comparing certain features of the MGC at different times. But we must start out from simple, idealized setups before we can achieve a better understanding of the more realistic scenario, involving an initially turbulent medium, magnetic fields, feedback from massive stars, gravitational collapse, completely accurate chemistry and thermal interactions, and so on.

1.1 Ionization Fronts

In general, ionization fronts are formed when massive stars are born within molecular gas clouds. The strong radiation almost instantaneously ionizes the gas in the stars' immediate surroundings, and heats it up as much as 1000–fold. This leads to a large jump in pressure which in turn leads to a pressure-driven expansion into the neutral medium in the form of a shell of swept up gas. At first this expansion is highly supersonic due to the steep pressure gradient across the ionization front. However, eventually the rate of recombinations inside the HII region balances the rate of ionizations – due to geometric dilution – at which point the front ceases to be super-sonic with respect to the ionized region and undergoes a transition from "R-type" to "D-type". The shell's radius at this time is approximately equal to the Stromgren radius, which is defined as:

$$r_s = \left(\frac{3s\mu_H^2}{4\pi\alpha^{(B)}\rho^2} \right)^{1/3},$$

(1.1)

where s is the ionizing luminosity of the star, μ_H and ρ are the mean mass per hydrogen atom and the density of the gas, respectively, and α^B is the recombination coefficient. The time at which the transition occurs is known as the Stromgren time, equal to r_s divided by

the sound speed in the ionized gas,

$$t_s = r_s/c_{II}. \tag{1.2}$$

The D-type front will continue to expand supersonically with respect to the ambient neutral medium for millions of years, leaving behind an increasingly large HII region.

HII regions have important implications for the global evolution of MGCs. Ionization fronts can disrupt parts of the MGC, preventing them from gravitationally collapsing to form stars. At the same time they can also cause the formation of over-dense clumps with an increased rate of star formation, especially when combined with MHD turbulence (§1.5). It is likely that HII regions lower the global rate of star formation in MGCs since much of the neutral gas that could collapse to form stars is swept up into a thin shell or driven off the cloud in an ionized wind. Nonetheless HII regions can have both a positive and negative influence on star formation rates in MGCs.

1.2   Blister HII Regions

In this paper we are particularly interested in the blister-type HII region. A sketch adopted from Krumholz & Matzner (2009) is shown in Fig. 1.1 comparing blister and symmetric HII regions.
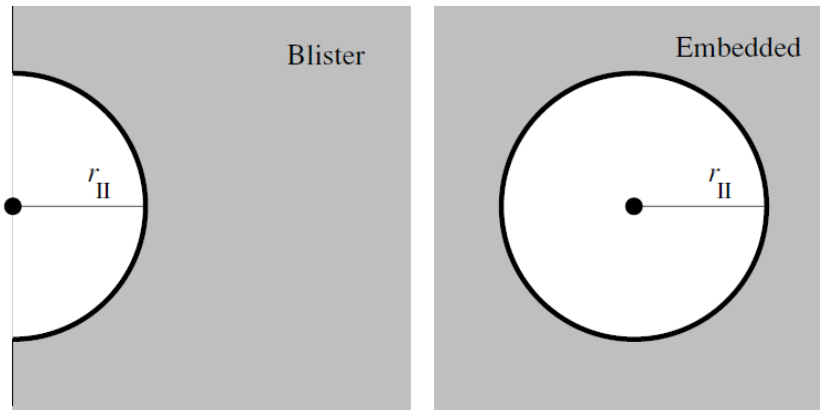
Figure 1.1: A sketch comparing the blister and symmetric HII regions (Krumholz & Matzner, 2009).

In the blister-case the star is situated next to the edge of the MGC, so the ionization front will eventually reach the edge of the cloud and burst a hole through which hot ionized gas will be able to stream out at extremely high velocities into the low-density ISM. In contrast with the symmetric case, the ionized gas within the HII region is not confined to the HII region, leading to a phenomenon known as the rocket effect which increases the expansion rate of the ionization front.

To understand this effect it is first important to note that as the D-type ionization front travels through the MGC, it sweeps up neutral gas since it travels above the neutral sound speed c_0. As a result the density within the shell is higher than its surroundings. At the ionized inner edge of the shell, the gas pressure therefore exceeds that in the lower density ionized gas closer to the star. Thus there will be a pressure-driven movement of gas away from the shell. This movement will be in the negative $\hat{r}$ direction, that is, in the direction opposite to the one in which the ionization front is expanding. This movement is

less restricted in the blister-case, since the gas is not confined to the HII region, so more gas can accelerate off of the ionization front, and analogously to a rocket traveling in air, more force is applied to the ionization front. Hence the ionization front will expand faster in the blister-case than in the spherically symmetric case, and consequently we would expect the kinetic energy to be higher as well.

1.3   Shell Radius

The radius of the shell as a function of time can be derived using conservation of momentum and some simplifying assumptions. If we assume that the pressure inside the HII region is vastly dominant over the ambient pressure in the neutral gas into which it is expanding at all times, and that the density within the HII region is approximately uniform, then we can obtain an equation of motion for the shell from momentum conservation. This equation of motion can then be solved by using a power-law similarity solution. We provide a derivation for both the symmetric and blister cases in Appendix A. In Spitzer (1978) there is a derivation of the symmetric case performed in a slightly different way, yielding a very similar solution. The solutions we find for the two cases differ only by a factor of $2^{2/7}$, and are provided below:

$$r_{sh} = r_s \left(\frac{7t}{\sqrt{12}t_s} \right)^{4/7} (spherical), \tag{1.3}$$

and

$$r_{sh} = r_s \left(\frac{7t}{\sqrt{6}t_s} \right)^{4/7} (blister). \tag{1.4}$$

How valid are the approximations we use? In reality, even though the assumption that the ambient pressure is negligible in comparison with the pressure inside the HII region is quite accurate at early times, the HII region internal pressure decreases as the HII region expands,

and so it becomes less accurate. Furthermore, even though the assumption that the density is uniform within the HII region for the symmetric case is valid, it is not necessarily quite as true for the blister-case where gas is free to stream out of the HII region into the interstellar medium. Hence the radius as a function of time will likely not match the analytic solution perfectly for all times, especially for the blister-case. In §3.3.1 we perform some calculations with our simulation data to see how pronounced these innacuracies in the analytic solution due to these approximations might be.

1.4   The Effect of Magnetic Fields

Magnetic fields are ubiquitous in molecular gas clouds. This is to be expected since a small fraction of the total atoms in MGCs are ionized, which gives rise to magnetic fields since moving charged particles produce a magnetic field. But what are the effects of adding in Magnetohydrodynamics into the model? Magnetic field lines resist being stretched, due to the Lorenz force, so we would expect them to restrict the expansion of the HII region in the direction perpendicular to them. This restriction would lower the kinetic energy imparted to the molecular gas cloud by the HII region. At the same time, MGCs have magnetic energy comparable to their kinetic energy (Crutcher, 1999), so it is important to look at the total energy in the cloud (kinetic plus magnetic) to understand how HII regions affect their turbulence and evolution. It is likely that although the magnetic fields limit the kinetic energy of the cloud in the MHD simulations, the total energy will actually be greater than for their non-MHD counterparts.

However, the addition of magnetic fields adds another layer of complexity to the analysis. Even though the expansion of the ionization front will be suppressed perpendicular

to the magnetic field lines, there will be MHD waves which can outrun the dense shell. In general there are three types of MHD waves: the slow magnetosonic wave, the Alfven wave, and the fast magnetosonic wave. The fast magnetosonic wave is formed due to the magnetic field lines acting as a restoring force in a direction perpendicular to them. Just as in the harmonic oscillator, this restoring force coupled with a density fluctuation moving across the magnetic field lines can give rise to a wave, with a velocity given by $v_f = \sqrt{v_A^2 + c_s^2}$, where $v_A = B/\sqrt{\mu_0 \rho}$ is the Alfven velocity and $c_s = \sqrt{kP/\rho_0}$ is the sound speed of the neutral gas.

Initially the D-type ionizination front is highly supersonic, but over time it can slow down enough that the fast magnetosonic wave will outrun it, disturbing neutral gas ahead of the ionization front, so that there is swept up material in between the fast magnetosonic disturbance and the ionization front. This has important implications for our results, as we discuss in Chp. 3.

Finally in the blister case the magnetic field lines act to guide the gas being ejected as it is photoionized, increasing the impulse it delivers to the cloud as it rockets away. In the symmetric case the gas is confined within the HII region and cannot rocket away, so this effect does not apply. Hence we would expect the kinetic energy for the blister MHD shell to be higher than for the symmetric MHD shell.

1.5   Magnetohydrodynamic (MHD) Turbulence

MGCs contain overdense regions within which stars form. These overdense regions can form due to magnetohydrodynamic turbulence, which provides density fluctuations, changing the balance between gravity and pressure within the cloud, and leading to localized

gravitational collapse (Stone et al., 1998). MHD turbulence is ubiquitous amongst MGCs, but what gives rise to it is poorly understood and is still an open research question. One mechanism that has been proposed is ionizing radiation (e.g., Gritschneder et al. 2009). We know that it takes about 2 crossing times for the turbulence to be dissipated (McKee & Ostriker, 2007), so the total energy produced by the ionization front must be comparable within this timescale to be able to counteract the dissipative forces and drive the turbulence. It is therefore important to study the efficiency with which HII regions are able to inject energy into GMCs.

1.6 Previous Studies and the Purpose of Our Research

In this paper we build on previous work by Krumholz & Stone (2007), which was the first study of the expansion of an HII region into a magnetized gas. The work we present here expands this effort to include blister-type HII regions, which form when an ionizing star is situated towards the edge of the MGC. There has been significant numerical research done on HII regions in recent years, but most of this research involved simplifying assumptions which lead to physically unrealistic results. However, following the work of Krumholz & Stone (2007), we include not only MHD in our simulations, but also radiative transfer, and we do not assume that the ionized gas is always in thermal or ionization equilibrium. The magnetic energy in MGCs is known to be comparable to the thermal and kinetic energies, and in §3.3.4 we will show that including a magnetic field has dramatic consequences for the total energy provided to the cloud by the HII region.

There have been several recent papers involving HII regions in a turbulent medium (e.g. Gritschneder et al. 2009 and Arthur et al. 2011). They produced results that looked

similar to observed features of HII regions, such as the prominent pillar-like structure of the Eagle Nebula. In our work we do not assume an initially turbulent medium – we are more interested in analyzing how efficient the different kinds of HII regions are at driving turbulence in the first place. Our work is therefore complementary to that of Gritschneder and Arthur.

2

Computational Methodology

The simulations are performed using the Athena 3D MHD code (Stone et al., 2008). Athena is a grid-based, static mesh refinement (SMR) code designed for simulating various Astrophysical MHD processes. It uses higher order Godunov methods, which are particularly efficient when used with static or adaptive mesh refinement, in combination with the constrained transport technique, which is used to ensure that the magnetic divergence is preserved to machine precision. In addition, to handle the ionizing radiation, we employ the radiation scheme first introduced in Krumholz & Stone (2007). We run all simulations on the Pleiades cluster at UCSC at 256^3 resolution using 64 processors for an average wall-time of 3 days per simulation.

2.1   The Ideal MHD Equations

Athena solves the equations of ideal MHD. In conservative form, they are:

$$\frac{\partial \rho}{\partial t} + \nabla \cdot (\rho \boldsymbol{v}) \quad = \quad 0 \tag{2.1}$$

$$\frac{\partial}{\partial t}(\rho \boldsymbol{v}) + \nabla \cdot (\rho \boldsymbol{v}\boldsymbol{v} - \boldsymbol{B}\boldsymbol{B}) + \nabla P^* \quad = \quad 0 \tag{2.2}$$

$$\frac{\partial \boldsymbol{B}}{\partial t} + \nabla \cdot (\boldsymbol{v}\boldsymbol{B} - \boldsymbol{B}\boldsymbol{v}) \quad = \quad 0 \tag{2.3}$$

$$\frac{\partial E}{\partial t} + \nabla \cdot [(E + P^*)\boldsymbol{v} - \boldsymbol{B}(\boldsymbol{B} \cdot \boldsymbol{v})] \quad = \quad \mathcal{G} - \mathcal{L} \tag{2.4}$$

$$\frac{\partial \rho_n}{\partial t} + \nabla \cdot (\rho_n \boldsymbol{v}) \quad = \quad \mathcal{R} - \mathcal{I} \tag{2.5}$$

$$\nabla \cdot \boldsymbol{B} \quad = \quad 0, \tag{2.6}$$

where ρ is the density and $\boldsymbol{v}$ is the velocity of the gas, $\boldsymbol{B}$ is the magnetic field, $P^* = P + (\boldsymbol{B} \cdot \boldsymbol{B}/2)$ is the total pressure, P is the gas thermal pressure, E is the total energy density, and ρ_n is the density of the neutral gas. Equation 2.1 is the continuity equation (conservation of mass), 2.2 is the conservation of momentum, where we have used the approximation that our fluid has no viscosity ($\nu = 0$), 2.3 is Faraday's law, or the induction equation, where we have set the magnetic diffusivity to zero ($\eta = 0$) since we are approximating that the magnetic field is frozen into the fluid, 2.4 is the conservation of energy equation, where $\mathcal{G}$ and $\mathcal{L}$ are the radiative heating and cooling terms, respectively, 2.5 is the continuity equation for neutral gas, and says that a change in the mass of neutral gas can only come through advection into other cells or through recombinations ($\mathcal{R}$) and ionizations ($\mathcal{I}$), and 2.6 comes from the non-existence of magnetic monopoles (it says that the magnetic field is divergence free). The heating and cooling terms, $\mathcal{G}$ and $\mathcal{L}$, will be discussed in more detail in §2.6.

2.2 Problem Setup

We set up a rectangular grid which runs from -25.0 to 25.0 pc in all 3 directions. For the spherical case, we place the star at the center of the grid, with $(x, y, z) = (0, 0, 0)$, and assume a constant background density of $n = 63.0$ atoms cm^{-3} across the whole domain. For the blister-type runs, we split the grid into two halves: all cells with $x < 0$ are of higher density, $n_{left} = 63.0$ atoms cm^{-3}, while all cells with $x > 0$ are of a low density, $n_{right} = 0.055$ atoms cm^{-3}, in order to put the two halves into pressure balance given the heating and cooling functions we are using, and we place the star at the center of the grid (at the boundary between the two regions). For the spherical MHD and the blister MHD runs we thread the initial magnetic field through the domain in the $\hat{x}$ direction. In addition, we perform one blister-type run with the initial magnetic field at $45°$ to the x axis and finally one run with the magnetic field in the $\hat{y}$ direction. In all MHD runs, the initial magnetic field is $B_0 = 3.0 \times 10^{-6}$ in the code units, which differ from cgs units by a factor of $\sqrt{4\pi}$, so that in cgs it is $\sqrt{4\pi}(3.0 \times 10^{-6})\mu G = 10.6\mu G$. A summary of the various runs and their magnetic field orientation is provided in Tab. 2.1.

A note on the blister type HII region setup: in reality it would clearly be a coincidence if the star was positioned right on the edge of the cloud. In reality blister HII regions are likely to form when a star is close to, but not directly on, the edge of the cloud. However ours is an instructive limiting case, since it is much harder to interpret and make sense of computational data that would result from a more realistic setup. It would be useful to extract as much information as possible from our idealized setup, and in a later paper expand our investigation to compare to the more realistic scenario.

Table 2.1: Problem Setup

Simulation Name	Type	Magnetic Field Setup
Hydro	Symmetric	None
MHD	Symmetric	$\hat{x}$ direction
Blister-hydro	Blister	None
Blister-mhd	Blister	$\hat{x}$ direction
Blister-mhd-vert	Blister	$\hat{y}$ direction
Blister-mhd-45	Blister	At 45° to the $\hat{x}$ direction

2.3 Configuration Parameters

The parameters relevent to our problem required to configure Athena so as to reproduce our results are summarized in Tab. 2.2. We refer the reader to the Athena manual for details. We configure Athena with the Roe solver based on the Godunov scheme in conjunction with the ctu integrator to produce the most accurate results, and we enable h-correction in order to eliminate carbuncle problems. The finite resolution of the grid produces extra viscosity on motions unaligned with the grid, so h-correction helps in that it adds an artificial viscosity along the grid to counterbalance this effect. We resort to using first order fluxes because higher order fluxes proved unstable at 256^3 resolution in at least some of our runs. Ionizing radiation is enabled and ion_point is selected since we treat this star as a point source.

Table 2.2: Configuration Parameters

Prefix	Parameter	Value
with	flux	roe
with	integrator	ctu
with	order	1
with	gas	hydro or MHD
with	eos	adiabatic
enable	mpi	
enable	h-correction	
enable	ion_point	
enable	ion_radiation	

2.4 Ionizing-Radiation Parameters

The parameters required to ensure that the time-step is not too large, and to treat the rays appropriately, are presented in Tab. 2.3. The details are described in Krumholz & Stone (2007). One simplifying technique we employ in treating the rays is known as the "on-the-spot" approximation (Osterbrock, 1999). In an optically thick medium, photons are absorbed almost instantaneously (or "on-the-spot") after being generated during recombination. Hence it is a good approximation to just have the effects of emission and absorption cancel each other out rather than having to push the re-emitted photons through the ray-tracing algorithm – which would significantly increase computational time. It is possible that the non-uniform density profile of the blister HII region (discussed in §1.3) can alter how accurate the "on-the-spot" approximation is (either in a positive or negative way), but we do not investigate either possibility in this paper.

Table 2.3: Ion-Radiation Parameters

Parameter	Value
time_unit	1.0
max_de_iter	0.1
max_de_therm_iter	0.1
max_de_step	10.0
max_de_therm_step	10.0
max_dx_iter	0.1
max_dx_step	10.0
tfloor	10.0
tceil	1.0×10^6
maxiter	100
ray_number	2
min_tree_level	2
rebuild_interval	5

2.5 Physical Parameters

The following parameters are all adopted from Krumholz & Stone (2007) and summarized in Tab. 2.4. We set the photoionization cross section to $\sigma_{ph} = 6.3 \times 10^{-18} cm^2$, which is the cross section for absorption of a photon at ionization threshold by a neutral hydrogen atom. The mean mass per hydrogen atom is $\mu_H \approx 2.34 \times 10^{-24}$ g, and the mean particle mass in the neutral gas is $\mu = 2.1 \times 10^{-24}$ g, appropriate for atomic gas.

Table 2.4: Physical Parameters

Parameter	Value
σ_{ph}	$6.3 \times 10^{-18} cm^2$
μ_H	$\approx 2.34 \times 10^{-24} g$
μ	$2.1 \times 10^{-24} g$
α_c	3.0×10^{-3}
α^B	$2.59 \times 10^{-13}(T/10^4 K)^{-0.7}\ cm^{-3}s^{-1}$
e_γ	$3.84 \times 10^{-12} ergs$
c_0	$5.74 \times 10^4 cm/s$
c_{II}	$8.7 \times 10^5 cm/s$
n_{left}	0.63 atoms cm^{-3}
n_{right}	0.055 atoms cm^{-3}
B_0	$10.6\mu G$

The carbon number fraction is $\alpha_c = 3.0 \times 10^{-3}$ (and we assume all carbon is singly ionized since its ionization potential is less than that of hydrogen). The energy yield per photoionization is $e_\gamma = 3.84 \times 10^{-12}$ ergs. The speed of sound in the dense half of the grid is $c_0 = 5.74 \times 10^4$ cm/s and $c_0 = 6.14 \times 10^5$ cm/s in the low density half, while in the HII region it is $c_{II} = 8.7 \times 10^5$ cm/s (Krumholz & Stone, 2007).

2.6 Heating and Cooling

The main source of heating in our simulation is due to photoionization of hydrogen by ionizing radiation. The photoionization rate summing over all sources is given by

$$\mathcal{G}_{ph} = \sigma_{ph} n_H \sum_n \frac{s_n}{4\pi |\mathbf{x} - \mathbf{x}_n|^2} e^{-\tau(\mathbf{X}, \mathbf{X}_n)} \tag{2.7}$$

(Krumholz & Stone, 2007), where n_H, the number density of hydrogen, and σ_{ph} are from table 2.4, s_n is the ionizing luminosity of the nth star, $\mathbf{x}$ is the position where the ionization is taking place, $\mathbf{x}_n$ is the position of the nth source, and τ is the optical depth to ionizing photons between $\mathbf{x}$ and $\mathbf{x}_n$, given by

$$\tau(\mathbf{x}, \mathbf{x}_n) = \int_{\mathbf{X}_n}^{\mathbf{X}} (\sigma_{ph} n_H) \, \mathrm{d}l. \tag{2.8}$$

The photoionization heating rate is just the photoionization rate multiplied by the energy per ionization, e_γ:

$$\mathcal{G} = e_\gamma \Gamma_{ph} = e_\gamma \sigma_{ph} n_H \sum_n \frac{s_n}{4\pi |\mathbf{x} - \mathbf{x}_n|^2} e^{-\tau(\mathbf{X}, \mathbf{X}_n)}. \tag{2.9}$$

There are several important sources of cooling for our simulation, including the recombination of hydrogen nuclei with electrons, free-free collisions, and line emission. When an electron recombines with a hydrogen nucleus, it loses kinetic energy, and a photon is

released which carries away energy from the system, cooling the gas. The cooling rate is proportional to n_{H^+} and n_e:

$$\mathcal{L}_{rec} \approx \Lambda_{rec} n_e n_{H^+}, \tag{2.10}$$

where the constant of proportionality is (Osterbrock, 1999),

$$\Lambda_{rec} \approx (6.1 \times 10^{-10} cm^3 s^{-1}) k_B T \left(\frac{T}{K}\right)^{-0.89}. \tag{2.11}$$

Another source of cooling is known as free-free emission, where free electrons get deflected and decelerated by charged ions in the gas. In this process the electrons lose kinetic energy, which is converted to low frequency radio photons to conserve energy, and these photons can leave the cloud, cooling the gas. Last but not least we take into account line-emission, which is an important source of cooling in many parts of the interstellar medium. Ion-electron collisions excite electrons to higher fine structure levels of many-electron atoms, which will eventually re-emit low energy photons, removing energy from the system. For our purposes the dominant coolants are the first and second excited states of N, O, and Ne, (Krumholz & Stone, 2007). With all of these contributions, the complete heating and cooling rates are

$$\mathcal{G} = e_\gamma \sigma_{ph} n_H \sum_n \frac{s_n}{4\pi |\mathbf{x} - \mathbf{x}_n|^2} e^{-\tau(\mathbf{X}, \mathbf{X}_n)} + n_H \Gamma_{KI}, \tag{2.12}$$

$$\mathcal{L} = \Lambda_{rec} n_e n_{H^+} + \Lambda_{ff}(T) n_e n_{H^+} + \Lambda_{KI}(T) n_H^2 + \Lambda_{line}(T) n_e n_{H^+}, \tag{2.13}$$

where we adopt the heating and cooling rates from Koyama & Inutsuka (2002) for neutral gas, and from Osterbrock (1999) for partially ionized gas.

3

Results

3.1 Symmetric Simulations

We begin our analysis by revisiting the extensively studied classic - the symmetric HII region - where the star is situated deep within the cloud.

3.1.1 Non-MHD Run

As expected, in the absence of a magnetic field, the ionization front expands in a spherically symmetric shell as shown in Fig. 3.1, rows 1 and 2. We can see that the density of the shell increases over time and that virtually all the kinetic energy is contained within the thin shell that bounds the ionization front. The shell expands slower than the analytic approximation (Eqn. 1.3) predicts, a discrepancy that is most likely explained by the approximations used in deriving the analytic solution. (We investigate this further in §3.3.1).

We define the shell radius as the average radius of all cells whose density is greater

than or equal to $1.1\rho_0$, where ρ_0 is the initial density defined in Tab. 2.4. We plot the radius vs. time in Fig. 3.2. This is a convenient way of defining the radius because the thin shell is a density fluctuation resulting from the sweeping up of neutral gas by the ionization front. For the non-MHD run this singles out the thin shell, but as we shall see in the following section, this is not always true for the MHD run.

3.1.2   MHD-Run

In the presence of the magnetic field, the expansion of the ionization front is strongly suppressed perpendicular to the magnetic field lines, so that over time the shape of the symmetric-MHD HII region resembles a football, as seen in Fig. 3.1, rows 3 and 4. The average radius is greater than in the non-MHD run as seen in Fig. 3.2, due to the fast magnetosonic wave leading the ionization front as discussed in §1.4. From row 3 of Fig. 3.1, it is apparent that at 0.5 Myr - corresponding to the first column of the figure - the MHD disturbance is just beginning to take the lead in front of the ionizing shell. By 1.5 Myr this disturbance is one of the most prominent features of the plot.

The radius of the shell is defined using the same criteria as §3.1.1, but in this case it encompasses the material contained in between the ionization front and the fast magnetosonic disturbance. Interestingly the resulting expansion rate, which is greater than for the hydro run, matches the analytic approximation (Eqn. 1.3) quite well, but this is probably just a coincidence.
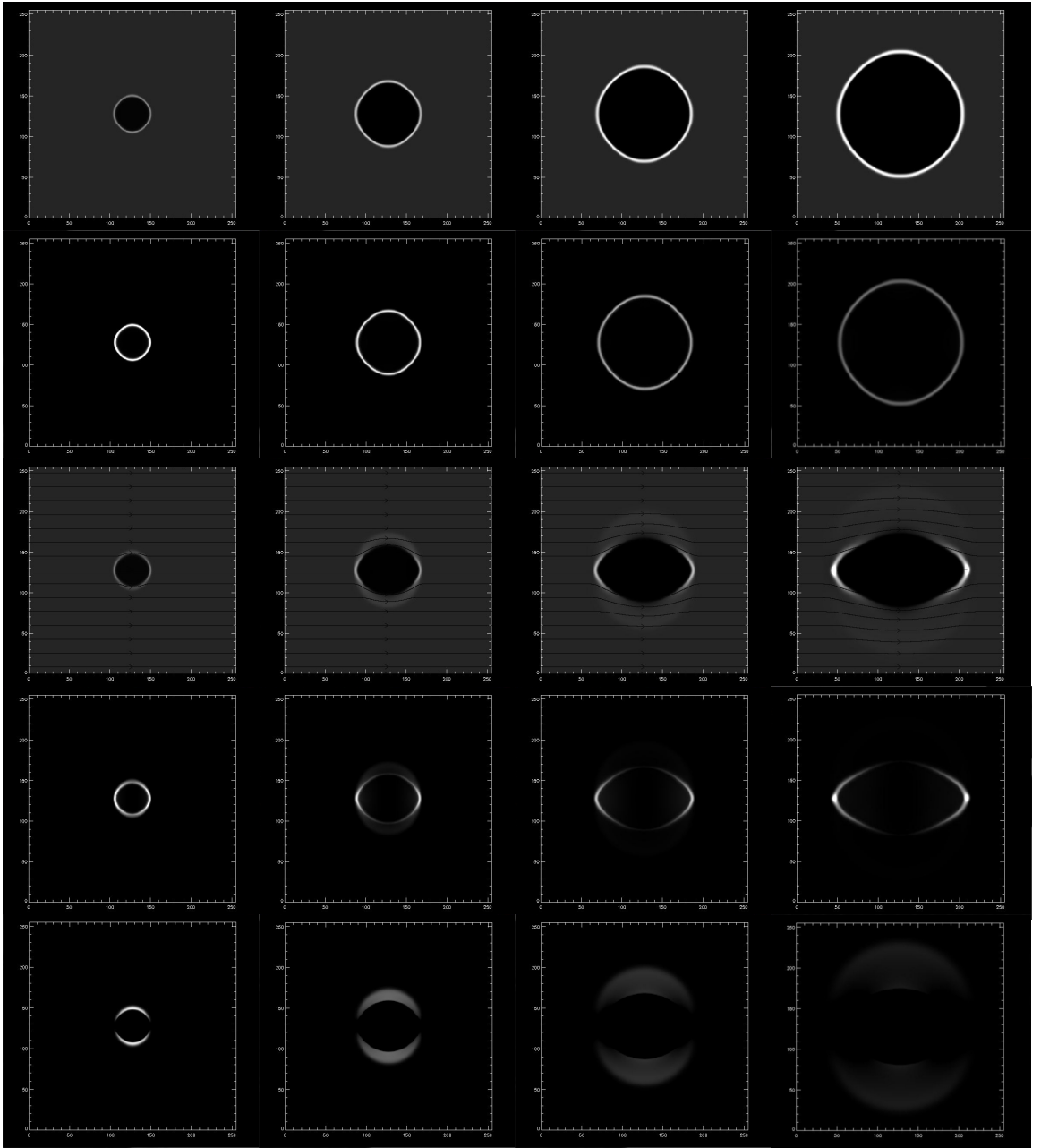
0.5 Myr   1.5 Myr   3 Myr   5 Myr

Figure 3.1: Slices in the $z = 0$ plane taken from the spherical-hydro and spherical-MHD runs. The 1st, 2nd, 3rd, and 4th columns correspond to 0.5, 1.5, 3.0, and 5.0 Myr into the simulation, respectively. The 1st and 2nd rows display the density and kinetic energy density of the symmetric-hydro simulation, while the 3rd, 4th and 5th rows display the density, kinetic energy density, and magnetic energy density minus initial magnetic energy density, respectively, for the symmetric-MHD simulation. The magnetic field lines are plotted in the 3rd row on top of the symmetric-MHD density slices.
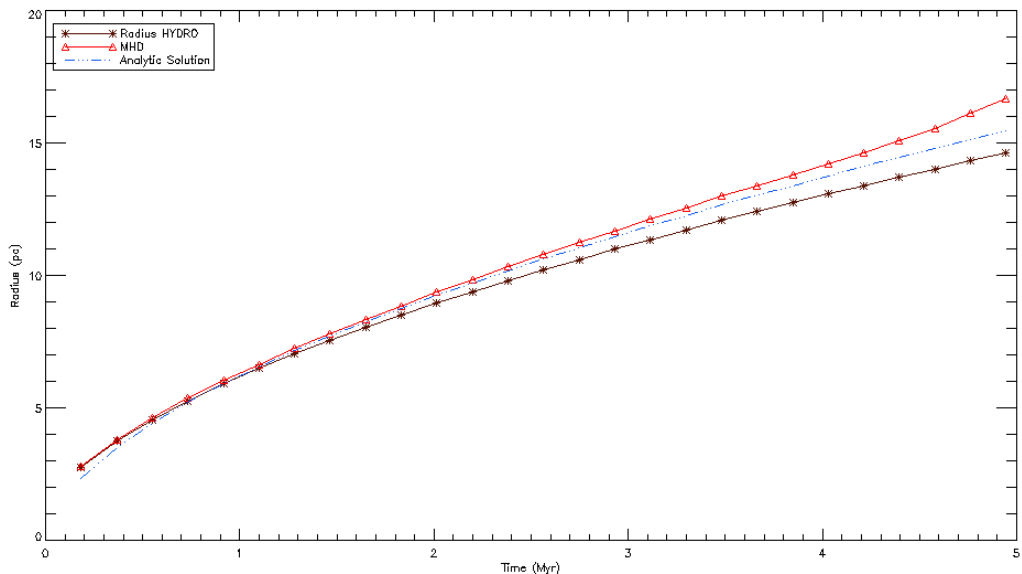
Figure 3.2: Radius vs. time for the symmetric-runs. The blue dashed curve represents the analytic solution (Eqn. 1.3).

This definition explains what is seen in the symmetric-radius plot comparing the expansion of the shell of the MHD to the non-MHD run 3.2. At $t < 0.5Myr$, the average radii of the two runs are virtually indistinguishable, but around 0.5 Myr the ionizing shell slows down enough that a fast magnetosonic wave disconnects from it and starts contributing significantly to the average radius of the MHD-run, so that by 1.5 Myr the radius of the MHD run is about 0.25 pc greater, and by 5 Myr it is about 2 pc greater.

Most of the kinetic energy in the MHD-run is contained in the thin shell, similar to the non-MHD run, but there is also some kinetic energy carried by the MHD disturbance ahead of the ionization front as seen in Fig. 3.1 row 4. This kinetic energy is greatest during the initial stages of the wave disconnecting from the ionization front, but this energy gets spread over an increasingly large area over time such that it is barely noticeable by

3 Myr. Virtually all of the magnetic energy added to the cloud due to the HII region, $\Delta B = ((Bx)^2 + (By)^2 + (Bz)^2)/2 - ((Bx_0)^2 + (By_0)^2 + (Bz_0)^2)/2$, where Bx_0, By_0, Bz_0 is the initial magnetic field strength in the x, y, and z directions, respectively, is contained in the MHD disturbance, as pictured in Fig. 3.1 row 5. This result implies that the magnetic energy added to the cloud probably depends more strongly on the size of the region between the ionization front and the leading magnetosonic wave than on the expansion rate of the ionization front. Thus we expect that the magnetic energy for the blister runs presented in §3.2 might be smaller than in the embedded run even though the ionization front expands at a faster rate in the blister case.

3.2 Blister-Type HII Simulations

3.2.1 No Magnetic Field

First we look at the blister-type scenario where there is no magnetic field present, in order to be able to better understand what effects the addition of a magnetic field has on the HII region.

Density and kinetic energy slices of the computational grid are presented for 0.5, 1.5, and 5 Myr of this run in Fig. 3.3. Initially the expansion into the dense half resembles the expansion in the symmetric case – the ionization front shell is almost identical to the left-hemisphere of the spherical shell in the symmetric-non-mhd simulation (Fig. 3.1). Over time, however, the deviation from symmetry becomes increasingly apparent. By 1.5 Myr there are slivers of the dense shell that extend further in the $\hat{y}$ direction – this effect is easiest to see from the kinetic energy plot in row 2 of the same figure. This extension will contribute significantly to the effective radius as we will show in §3.3.
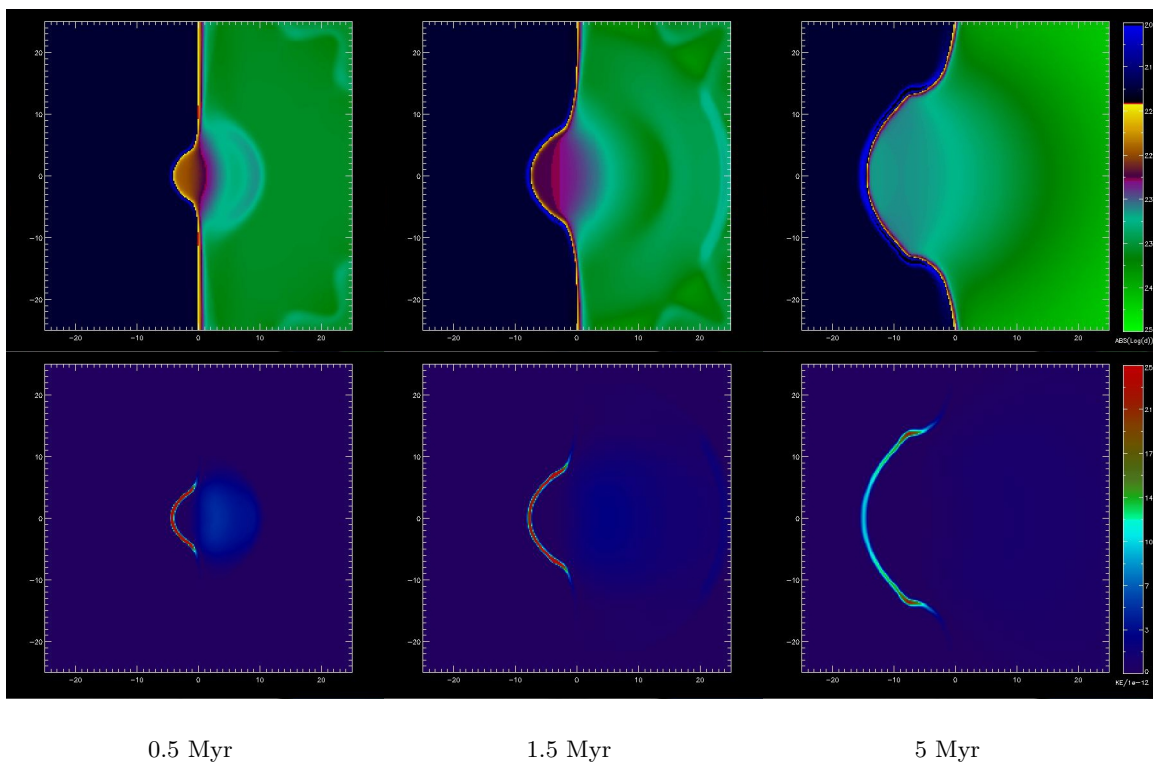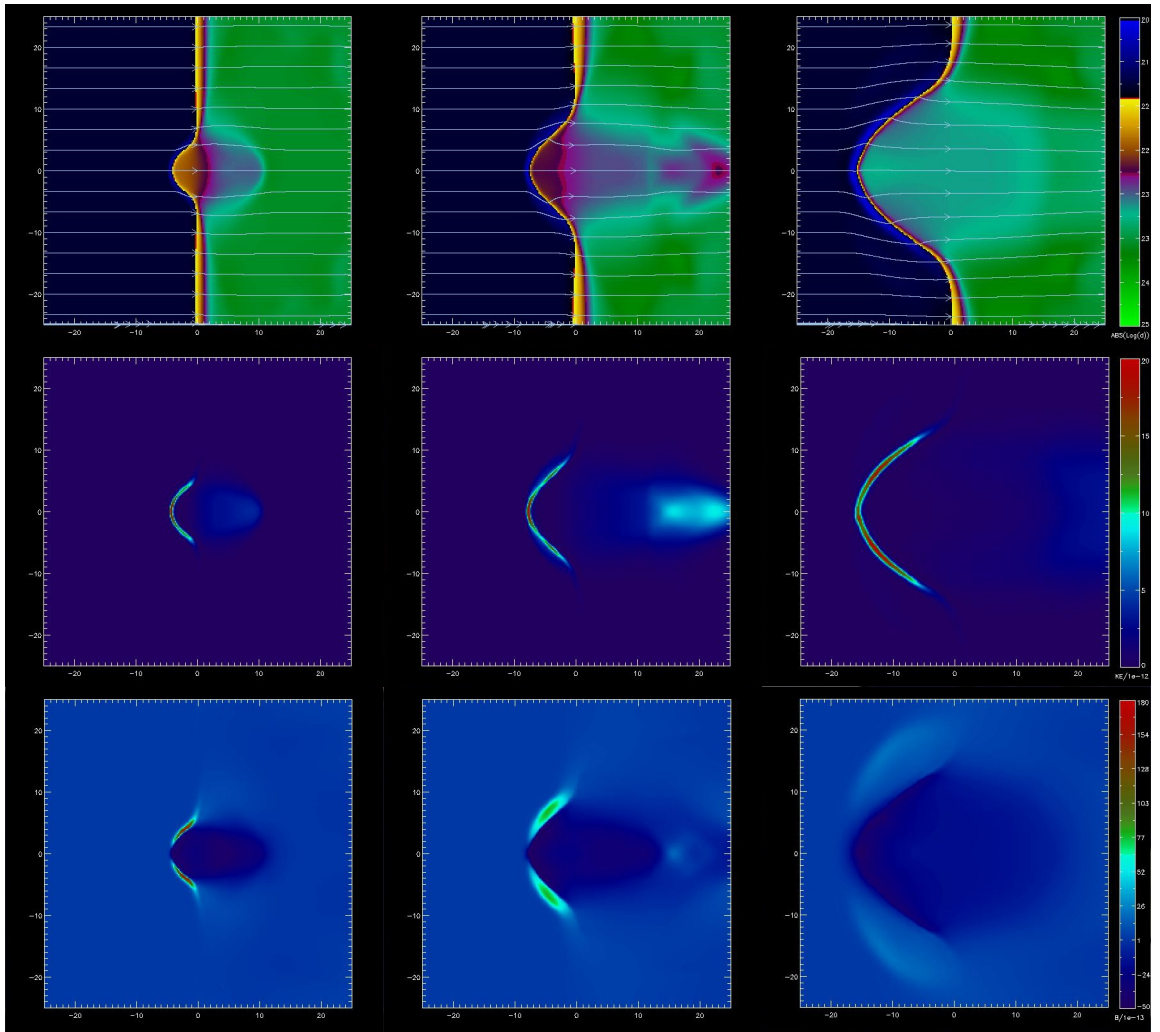
0.5 Myr   1.5 Myr   5 Myr

Figure 3.3: The blister-hydro run: the 1st row are the density slices while the 2nd row contains the kinetic energy density. The density is plotted on a log scale so that effects in the low-density part of the computational domain can be distinguished.

The density of the shell increases as a function of time as more neutral gas is swept up by the shock front, while the kinetic energy density within the shell constantly decreases due to the expansion rate becoming smaller over time. Furthermore, just as in the symmetric case, virtually all of the kinetic energy is concentrated in the shell, with the almost negligible exception of a spherically-symmetric jet of gas blowing out of the cloud at high speeds. From the figure it is apparent that although this low-density material covers a wider area than the dense shell, its average kinetic energy density is dozens of times lower than the kinetic energy density within the shell.

3.2.2 Magnetic Field Oriented Perpendicular to the Edge of the Cloud

This setup is the most useful for seeing the effects of adding a magnetic field; it is easy to compare with the blister-hydro run. The first observation is that the expansion of gas – both in the dense and low density portions of the computational domain – is limited in the directions perpendicular to the magnetic field, as expected (Fig. 3.4). The gas gushing out of the cloud is much more streamlined and dense.

0.5 Myr   1.5 Myr   5 Myr

Figure 3.4: The blister-mhd run: same as Fig. 3.3 except the change in magnetic energy density is plotted on a scale shifted to lower values than the kinetic energy density by a factor of 10 in row 3.

A chunk of hot gas resembling a bullet bursts out of the cloud and by 1.5 Myr has already reached the edge of the grid, implying a speed of 15-20 km/s, so a significant amount of kinetic energy is both gained and lost over the course of the simulation. Since we are concerned with the effects of the ionization front inside the cloud, it is important for

our analysis not to take this fluctuation – which occurs outside of the cloud – into account when comparing to the other runs.

The kinetic energy in the dense half is all concentrated in the shell, which is very similar in structure to the shell in the blister-hydro case (row 2 of Fig 3.4). However, the shell is more oblate, and in contrast to the blister-hydro shell, it actually gains kinetic energy density over time, rather than losing it. Thus one of the most important MHD effects in the blister-mhd case is that the magnetic field changes the nature of the expansion over time (as we will see in §3.3), by collimating the jet of gas streaming out of the cloud (as discussed in §1.4). Another interesting result is that within the HII region there is a net loss of magnetic energy, as depicted by the dark tones (corresponding to a negative change in energy) of the central region contained within the ionizing shell.

As predicted in §3.1.2, most of the added magnetic energy is contained within a disturbence bounded by the ionization front and the fast magnetosonic wave front, and this is confirmed by the change in magnetic energy density plots in row 3 of Fig. 3.4. The disturbance has a behavior similar to that in the symmetric case - it is highly concentrated at first with large values of the change in magnetic energy density, but gets diluted over time as it covers an increasingly wide area.

3.2.3   Magnetic Field Oriented Parallel to the Edge of the Cloud

We refer to this run as the "blister-vert" run, where "vert" stands for magnetic field lines oriented in the $\hat{y}$ direction. Initially, similar to the blister-mhd case, a jet of gas bursts out of the cloud as seen in Fig. 3.5. However the jet is not streamlined and it is not propelled at high velocities through the low-density medium – its motion is highly

suppressed by the magnetic field perpendicular to it – and the magnetic field gets stretched the most out of any of the runs.

<div align="center">
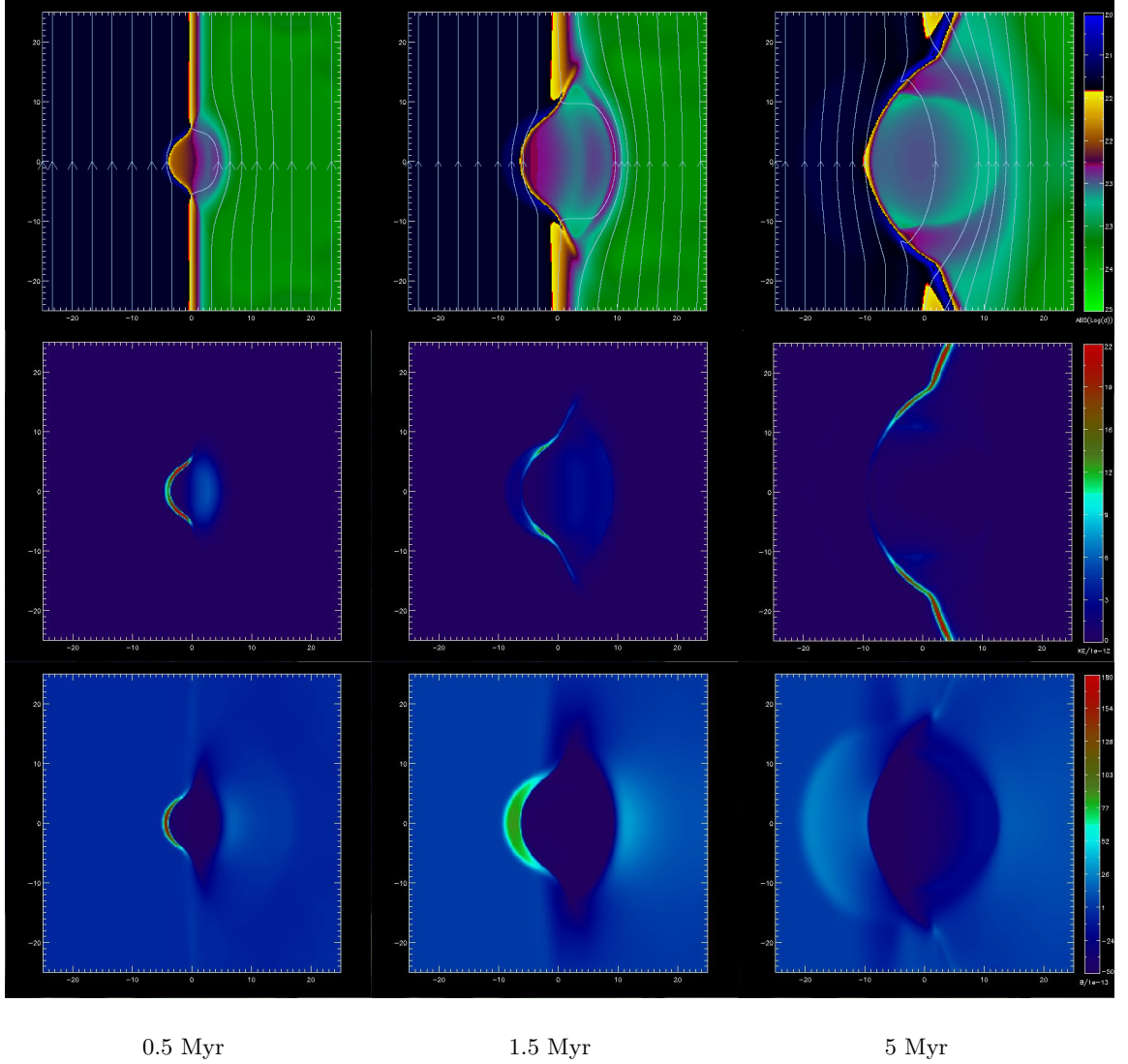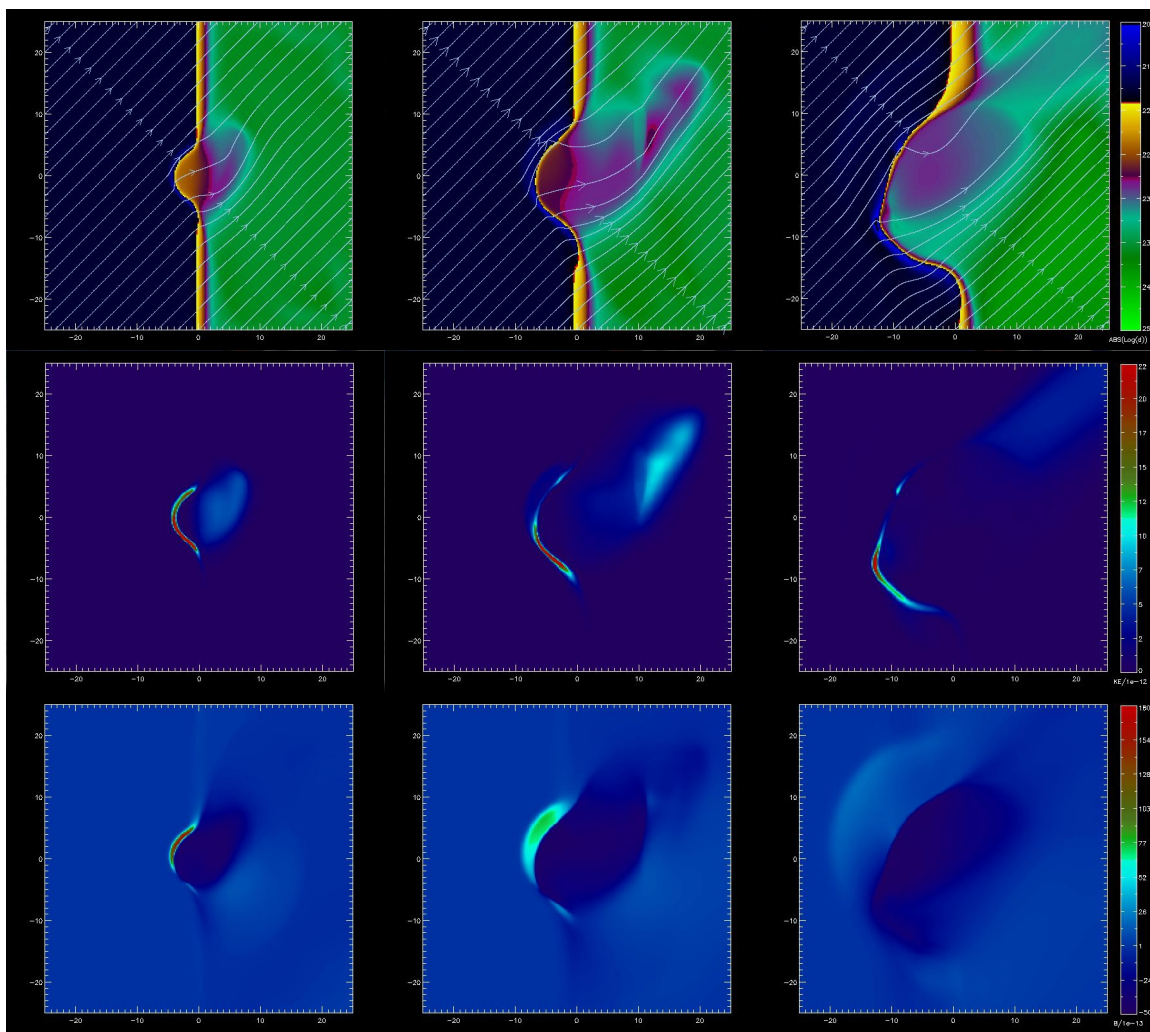0.5 Myr   1.5 Myr   5 Myr
</div>

Figure 3.5: The blister-vert run. All the plots and colorscales are the same as in Fig. 3.4.

The kinetic energy of the cloud is concentrated in the shell just as for the other runs but the magnetic field's suppression of the shell's motion in all but the vertical direction transfers most of the kinetic energy from the spherical part of the shell to the slivers of dense gas protruding into the low density medium by the end of the run (2nd row). The magnetic

energy density is plotted in row 3 of Fig. 3.5. As expected, since the ionization front is slow to expand perpendicular to the magnetic field lines, the fast-MHD disturbance disconnects from the front earlier than in any other simulation, resulting in a very prominent density fluctuation leading the ionization front.

3.2.4   Magnetic Field Oriented at $45°$ to the Edge of the Cloud

This simulation is a perfect blend of the properties of the blister-mhd and blister-vert runs. As seen in Fig. 3.6, the magnetic field lines limit the expansion of the front perpendicular to them, but do not prevent the front from travelling at a sizeable velocity parallel to them. The result is an HII region that has rectangular structure.

0.5 Myr   1.5 Myr   5 Myr

Figure 3.6: The blister-vert run. All panels are the same as in Fig. 3.4.

3.3   Comparison of the Symmetric and Blister Simulations

In this section we compare properties such as the radius, kinetic, magnetic, and total energies of the various simulations.

3.3.1 Expansion of the Ionization Fronts

As discussed in section 3.1, we define the shell radius as the average radius of all cells whose density is greater than or equal to $1.1\rho_0$, where ρ_0 is the initial density defined in Tab. 2.4. This means that for MHD-enabled runs, the radius of the shell will contain the contribution from the material in between the ionization front and the fast magnetosonic wave front. As expected, the blister-hydro case has the fastest expanding shell, as seen in Fig. 3.7. It is followed by the blister type runs with the 3 various magnetic field orientations (of which the blister-mhd radius is greatest for most of the simulation, but the blister-mhd-vert run catches up by the end), and these are followed closely by the symmetric-mhd run. The slowest expanding front, as expected, is the symmetric-hydro run.
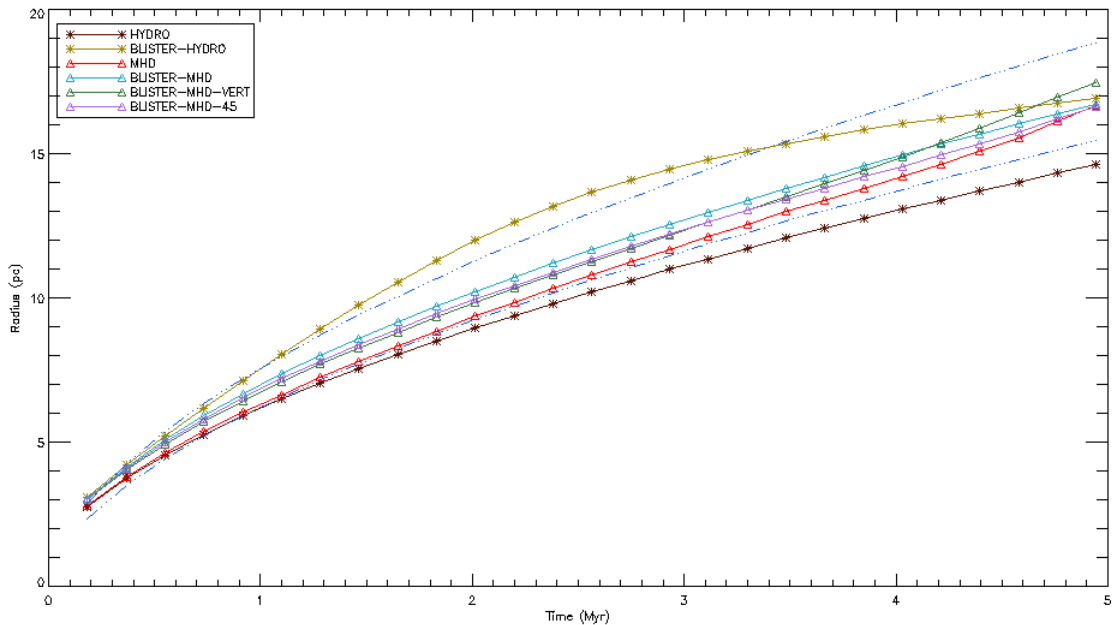

Figure 3.7: The mass averaged radii of all the runs. The blue-dashed curves represent the analytic solutions.

An interesting result is the shape of the blister-hydro curve. It starts out on par

with the analytic solution (Eqn. 1.4), takes the lead around 1 Myr, but comes back down even lower than the analytic solution around 3.2 Myr. In reality the blister-hydro curve is a bit misleading because it turns out that the spherical portion of the blister-hydro shell travels significantly slower than the analytic solution predicts. This is shown in Fig. 3.8, where we have calculated the radius of the blister-hydro shell by only considering gas along the $y = z = 0$ line. The spherical part of the shell expands just a bit faster than the symmetric shell. This implies that the slivers of the shell that extend in the $\hat{y}$ direction along the interface (as seen in Fig. 3.3) contribute significantly to the radius of the blister hydro curve. This is most likely the reason behind the discrepancy in curvature between the blister-hydro curve and its analytic solution; in the early-mid stages of the simulation the slivers expand faster in the y-direction than the spherical part of the shell expands in the radial direction, but towards the later stages the expansion of the slivers in the y-direction slows down dramatically and the curve becomes flatter than the analytic solution.

While this may explain the shape of the curve, it does not explain why the blister-hydro shell seems to expand at a rate comparable to the symmetric-hydro shell, rather than faster as predicted by the analytic approximation.
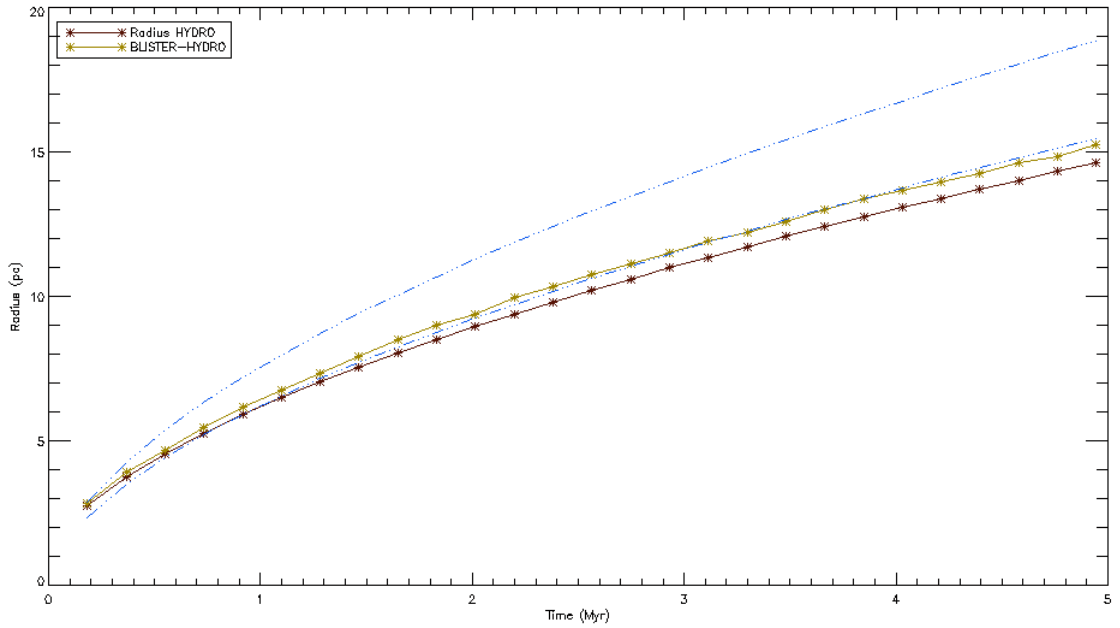
Figure 3.8: The radius for the blister-hydro run computed by only considering gas along the $y = z = 0$ line. The blue-dashed curves are the same as in Fig. 3.7.

This might be partly due to the approximation that the ambient pressure is negligible used in deriving the analytic approximation, as described in §1.1. This can be checked through a simple calculation. Using the parameters in Tab. 2.4, we can calculate the ionizing luminosity of the star from the formula for the Stromgren radius (Eqn. 1.1). This turns out to be $s = 5.3 \times 10^{47} ergs/s$. We want to compute the pressure of the HII region and the ambient medium and take the ratio of the two. The pressure of the HII region is given as $P_{II} = \rho_{II} c_{II}^2$, and similarly the pressure of the ambient medium is $P_0 = \rho_0 c_0^2$, where ρ_{II} and ρ_0 are the densities of the HII region and ambient medium, respectively, while c_{II} and c_0 are the sound speeds of the HII region and ambient medium , respectively. To find ρ_{II} at a certain radius, we invoke Eqn. 1.1 again. At 1 Myr the radius of the blister-hydro ionization shell is about 7 pc, which gives $\rho_{II} = 1.46 \times 10^{-23}$, and at 3 Myr, the radius

is about 14 pc, which gives $\rho_{II} = 5.2 \times 10^{-24}$ (where we have used $c_{II} = 8.7 \times 10^5$ cm/s and $c_0 = 5.74 \times 10^4$ cm/s from Tab. 2.4). Using these densities we find that at 1 Myr the percentage of ambient to HII region pressure is $\approx 4.4\%$, and at 3 Myr it is $\approx 12.3\%$. Thus although the approximation of HII region pressure dominance works quite well at early times, by 3 Myr it is not quite as accurate, and this discrepancy can cause some of the observed flattening of the blister-hydro curve late in the run.

Another problem with the analytic solution for the blister-case is that it assumes that the density is the same as in the symmetric HII region. This is not quite true since in the blister-case the gas is free to escape from the HII region out of the cloud, which is exactly what we observe happening in Fig. 3.3. The D-type ionization front travels below the sound speed of the HII region, so gas inside the symmetric HII region has time to spread out and achieve a uniform density. However in the blister-case the density is lower than in the symmetric case inside the HII region as we show in Fig. 3.9. Towards the beginning of the run the density in the blister case is $\approx 25\%$ smaller than in the symmetric case, a difference which can contribute to the deviation of the blister-hydro run from the analytic solution seen in Fig. 3.7.
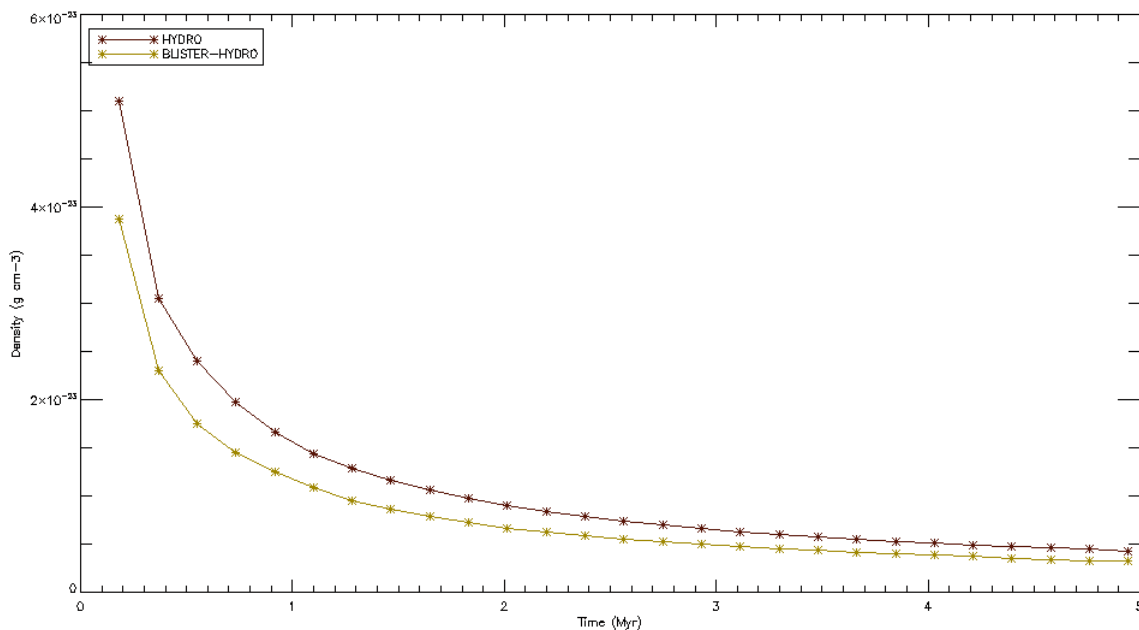
Figure 3.9: The density inside the hydro and blister-hydro HII regions plotted over time.

Another important result is how similar the expansion curves are for all the MHD simulations (Fig. 3.7). This is due to the fact that, at late times, the radius is effectively set by the fast magnetosonic fluctuation leading the ionization front. Thus in all the MHD cases, the radius is determined not only by the speed of the actual ionization front, which varies between the cases, but also by the fast magnetosonic speed, which does not. In §3.1.2, we observed that the symmetric-MHD run had a faster expansion curve than the symmetric-hydro run. From Fig. 3.7, we can see that the blister-type MHD runs have a higher base expansion rate than the symmetric-case due to blister-type effects discussed in §1.1, but the fixed value of the fast magnetosonic speed serves to ensure that the shapes of the curves are virtually the same at late times.

3.3.2 Kinetic Energy

We plot the total kinetic energies of the various runs in Fig. 3.10. We do not use all the cells in the computational domain to calculate the kinetic energy, but only those cells with a density $\rho > 0.9\rho_0$, where ρ_0 is the initial density from Tab. 2.4. We apply this condition to ensure the low density part of the grid does not get included in the analysis for reasons discussed in §3.2.2.
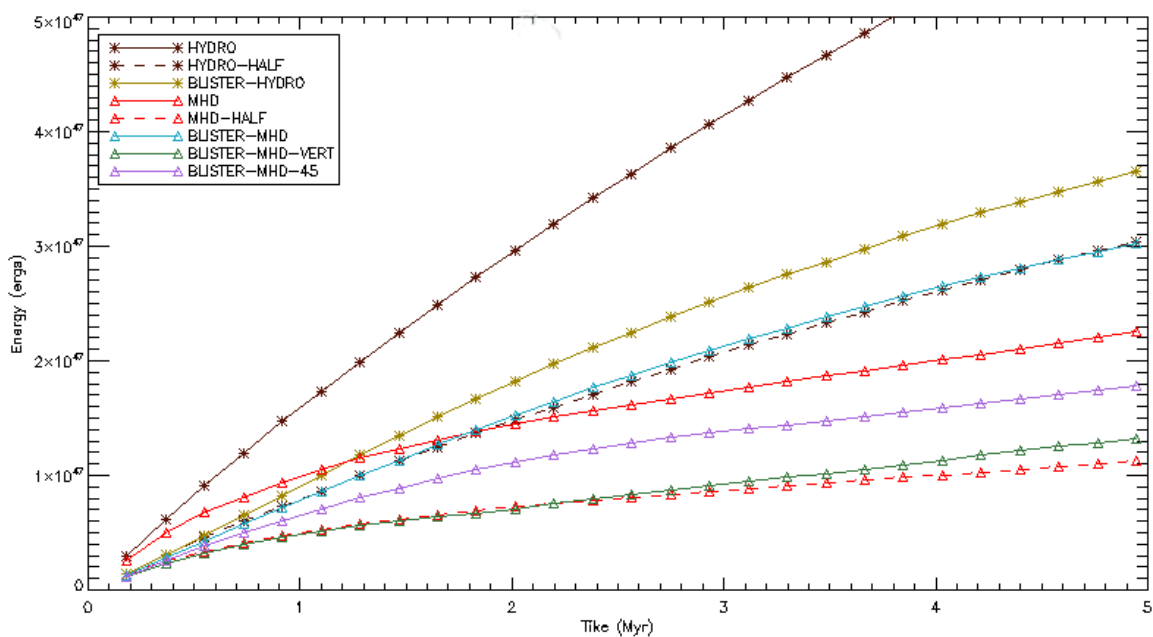

Figure 3.10: The total kinetic energy of all the runs. The kinetic energy is calculated only considering cells whose density is greater than 90 % of the initial density. The dashed curves represent the hydro and mhd curves divided in half.

The hydro-run has the greatest total kinetic energy, followed by the blister-hydro, blister-mhd, blister-45, and blister-vert runs in decreasing order. As for the symmetric MHD run, it starts off with a higher kinetic energy than all but the hydro-run, but early

in the simulation, even before the 1 Myr mark, its kinetic energy diminishes significantly, becoming lower than the blister-mhd run by 2 Myr, even though it is expanding into twice as many dense cells. The dashed lines are just the hydro and MHD runs divided in half, plotted to demonstrate that if we look at the kinetic energy in only one half of the grid, the blister runs dominate over their symmetric counterparts. The MHD run divided in half has as little kinetic energy as the blister-vert run.

The result that the blister-hydro kinetic energy is lower than the symmetric-hydro kinetic energy is contrary to what we would expect to see based on the analytic solution. From Eqn's. 1.3 and 1.4, we see that the predicted blister radius is larger by a factor of $2^{2/7}$ than the symmetric radius for any fixed time. The kinetic energy of the shell is given by $E_{KE} = 1/2M\dot{r_{sh}}^2$, where M is the mass of the shell. The mass of the shell increases as r_{sh}^3, so the mass of the blister-hydro shell should be larger by a factor of $2^{6/7}$ than the symmetric shell mass. Thus E_{KE} should be larger by a factor of $(1/2)(2^{6/7})(2^{2/7})^2 = 2^{3/7}$ for the blister-hydro run, where the $1/2$ term is included to account for the fact that the blister-hydro shell is a hemisphere rather than a sphere. In §3.3.1 we showed that the spherical part of the blister-hydro shell actually expands significantly slower than the analytic solution predicts (Fig. 3.8). Thus if most of the kinetic energy is concentrated in the spherical part of the shell, the total kinetic energy for the blister-hydro run could be lower than for the symmetric-hydro run. This is indeed the case. As seen in Fig. 3.3 row 2, the slivers of the shell that expand in the $\hat{y}$ direction have very little kinetic energy density. Thus, even though they contribute significantly to the radius of the blister-hydro shell, the total kinetic energy is lower in the blister-hydro case than in the symmetric-hydro case.

An important result is that the blister-mhd kinetic energy curve does not flatten as

much as that of the spherical-mhd run. The radius plot (Fig. 3.7) seems to be at odds with this result since all the MHD runs have very similar expansion curves. However, the radius of the MHD curves depends more strongly on the fast magnetosonic disturbance than on the expansion rate of the thin shell, as discussed in §3.3.1. Hence this result should not come as a surprise and implies that the rate of expansion of the thin shell is significantly lower in the spherical-mhd case than in the blister-mhd case. Another reason why the blister-mhd run has more kinetic energy is because the blister shell does not get as thin due to compression in the $\hat{y}$ direction by the magnetic field lines as much as the spherical-mhd shell (Figs. 3.1 row 4 and 3.4 row 2).

Another way to compare the kinetic energy in the different runs is to examine the energy per unit mass in the swept up region. We plot this quantity in Fig. 3.11. The results are virtually the same as having divided the energy of the symmetric runs in half. The blister-hydro run has $\approx 24\,\%$ more specific kinetic energy than the hydro run by 5 Myr (compared to $\approx 14\,\%$ greater radius at the same time). The most interesting result is how much more specific kinetic energy the blister-mhd shell contains than the blister-vert and blister-45 runs – ≈ 2 times more by 5 Myr, and ≈ 3 times more than the MHD-run by 5 Myr.
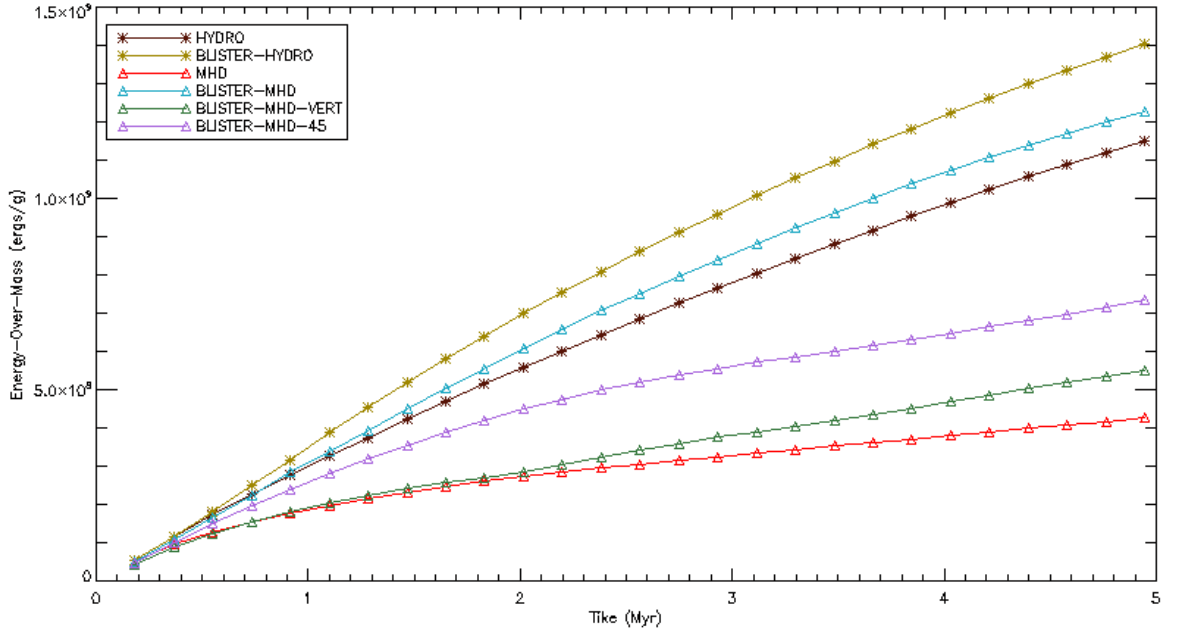
Figure 3.11: The specific kinetic energy of all the runs calculated only considering cells whose density is greater than 90 % of the initial density.

3.3.3 Magnetic Energy

For the magnetic energy, we expect the results to be opposite of those for the kinetic energy. The runs with the least kinetic energy should actually have the most magnetic energy since energy that does not go into motion is instead stored as distortions of the magnetic field. We present these results in Fig. 3.12. The dashed line is the MHD run divided in half for comparison.
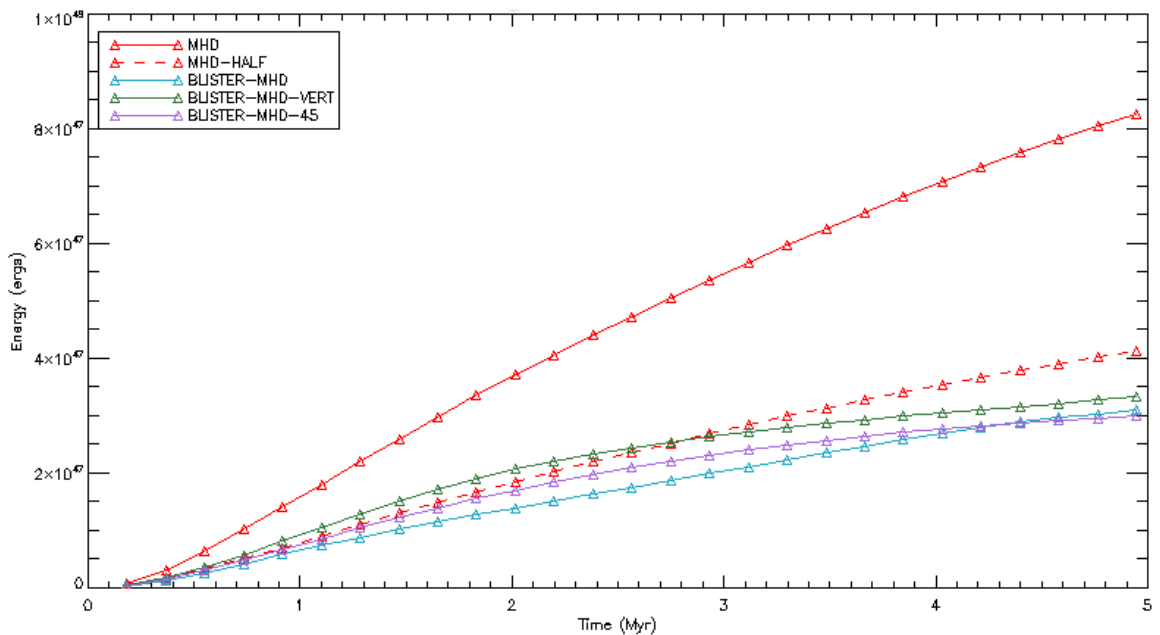
Figure 3.12: The total magnetic energy of all the runs. The magnetic energy is calculated only considering cells whose density is greater than 1.01 times the initial density. The dashed curve represents the mhd curve divided in half.

We only calculate the change in magnetic energy for cells with a density greater than 1.01ρ in order to limit ourselves to the shell and the fast-MHD disturbance, and to exclude the low density medium outside the cloud. The total change in magnetic energy ΔE_B is very similar for all the blister runs. For the MHD run divided in half, ΔE_B is about on par with ΔE_B for the blister-vert run, although its curve is significantly flatter and takes the lead after 3 Myr. Fig. 3.13 shows the specific change in magnetic energy $\Delta E_B/M$, where the sums include all cells with $\rho > 1.01\rho_0$. The curves all decline with time, which implies that the rate at which the magnetic energy changes is slower than the rate at which mass is swept up by the ionization front for all the runs.
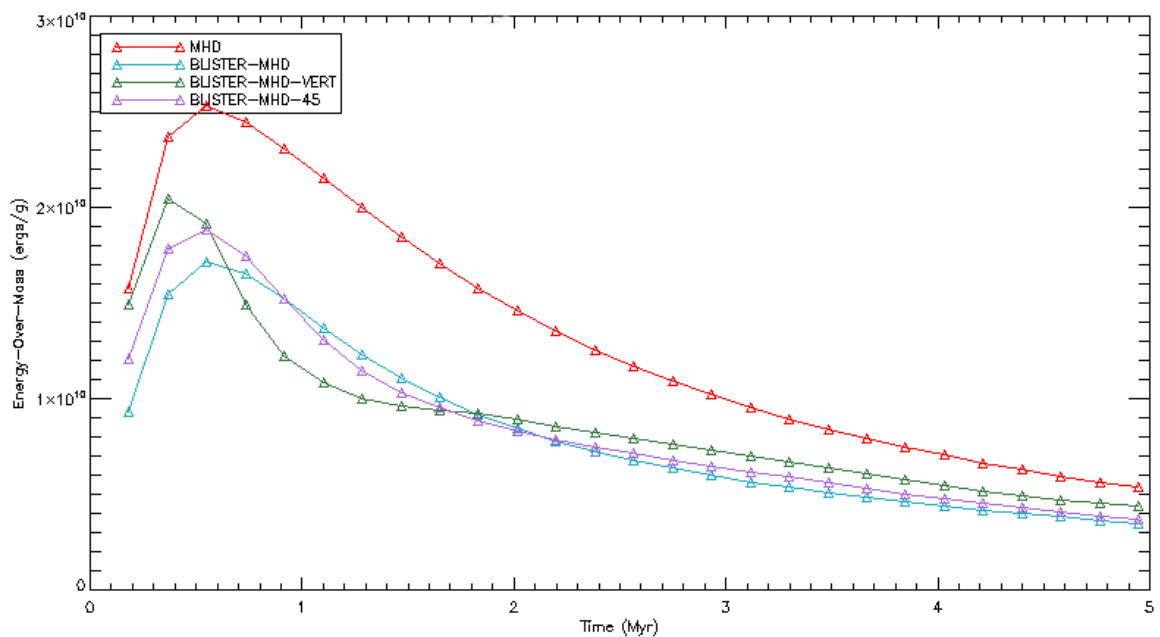
Figure 3.13: The change in specific magnetic energy.

3.3.4 Total Energy

In Fig. 3.14, we plot the total energy, that is, kinetic plus magnetic energy, for all the runs. For the hydro and blister-hydro runs, there is no magnetic energy of course, so this just consists entirely of the kinetic energy. Considering the dashed MHD and hydro curves, at 5 Myr the total energy imparted to the left half of the cloud is highest in the blister-mhd run, followed by the symmetric MHD run, then the blister-vert and blister-45 runs, then the blister-hydro, and finally the hydro run. The blister-mhd run has about the same total-energy as the other blister runs until about 1.5 Myr, at which point it splits from the other blister runs and by 5 Myr has $\approx$ 30 % more total energy. Comparing to the blister-hydro run, it is clear that magnetic effects are of great importance with respect to the total energy of the cloud. By 5 Myr, the blister-mhd run has about twice as much

energy as the blister-hydro run, and the blister-vert and blister-45 runs have about $\approx 30\ \%$ more energy.
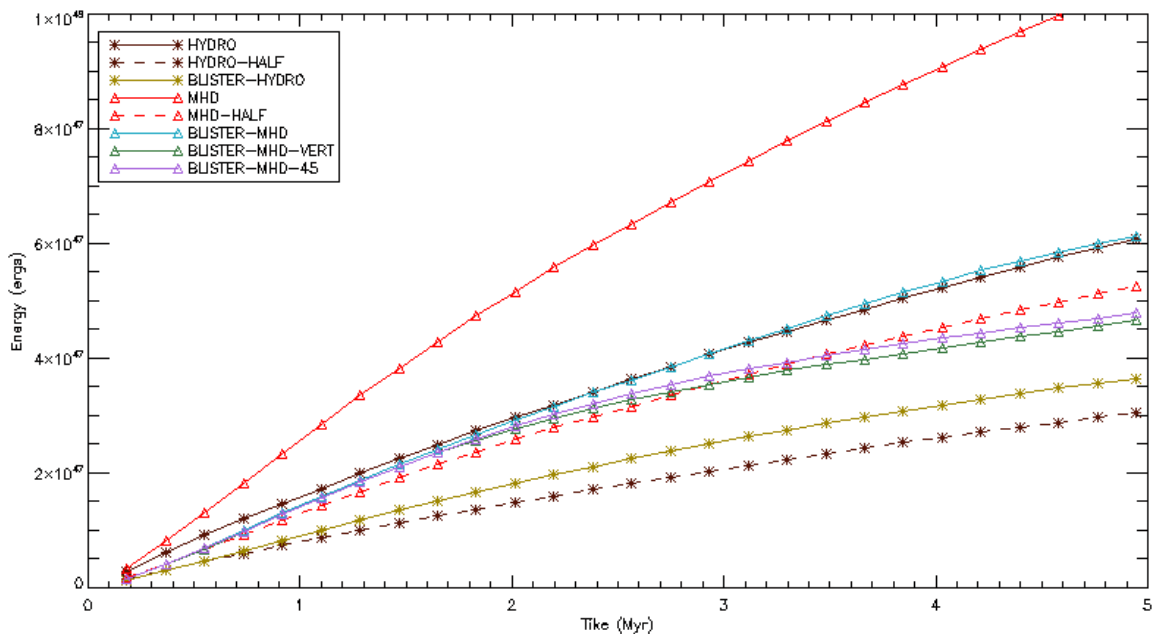

Figure 3.14: The total energy of all the runs. The dashed curves represent the hydro and MHD runs divided by a factor of two.

In terms of the total energy injected into the whole cloud, the winner is the symmetric MHD run by a large margin. However if only half of its energy is considered, the blister-mhd run with an initial magnetic field parallel to the edge of the cloud wins out by only a small margin. The other two blister-mhd runs have total energies very similar to the symmetric MHD half run. The blister-mhd run has significantly more total energy than either of the hydro runs. The reason for this is that all the lost kinetic energy for the MHD run has to go somewhere, and it gets stored in the magnetic field, with all the gained magnetic energy contained in the fast magnetosonic disturbance. It turns out that the symmetric MHD run is a bit more efficient at storing magnetic energy than the blister-MHD

runs towards the late stages of the simulation (the symmetric MHD half plot has $\approx 30\%$ more magnetic energy by 5 Myr than the blister-mhd run, Fig. 3.12).

To emphasize just how important MHD effects are to the energetics of the cloud, and hence explain why the MHD runs are so dominant over the hydro runs in terms of total energy, we look at the ratio of kinetic energy lost to magnetic energy gained in going from MHD to hydro for the blister-mhd run. It has only $\approx 20\%$ less kinetic energy ($\approx 6\times 10^{46} ergs$) than the blister-hydro run, so that the magnetic field lines do not limit the expansion of the blister-mhd HII region very efficiently (§1.4). Of course the blister-mhd run also has magnetic energy as opposed to the blister-hydro run, and the amount of added magnetic energy it has by 5 Myr is $\approx 3 \times 10^{47} ergs$, so the blister-mhd run gains 5 times as much energy as it loses compared to the blister-hydro run.

4

Conclusions

We have performed the first numerical study of the blister type HII region expanding into a magnetized medium. Our main interest is to see how efficiently a magnetized blister type HII region imparts energy into the cloud in comparison with a symmetric HII region, and in comparison to non-magnetic HII regions. We draw the following conclusions:

(i) The boost to the expansion rate of the ionization front in the blister-hydro case over the symmetric case is slightly less than the prediction of the analytic approximation (Eqn. 1.4). However, the dense shell of swept up material is not entirely spherical (Fig. 3.3 row 1). It has a spherical part that expands much slower than the analytic blister solution as well as thin tails oriented parallel to the edge of the cloud, which contribute to the radius of the whole shell. Most of the kinetic energy is contained in the spherical part of the shell, so the tails only make a small contribution to the energy budget. We find that the increase in kinetic energy for the blister hydro case relative to the symmetric hydro case is less than that predicted by the analytic approximation (Eqn. 1.4), suggesting that this approximation could be improved by adjusting it to better fit our results.

(ii) The expansion rate of all the MHD runs is very similar (Fig. 3.7). The blister runs get a slight boost over the symmetric run, but mostly the radius is determined by the material in the region between the fast magnetosonic and ionization fronts. But this material does not contain much kinetic energy in comparison with the dense shell (e.g. Fig.'s 3.1, 3.4, 3.5, 3.6), so the kinetic energy for the MHD runs is lower than for the hydrodynamic runs.

(iii) Comparing magnetized blister and symmetric HII regions, the blister cases have more kinetic energy but less magnetic energy, for reasons discussed in §1.4 and demonstrated in Fig.'s 3.10 and 3.12. The total energy is greatest in the symmetric case, so HII regions of this type make the greatest contribution to the total energy budget of a cloud, but if the kinetic energy proves more important than the total energy for the purpose of driving turbulence, then blister HII regions will be more effective.

(iv) One of the main results of our study is that any type of MHD HII region has much more total energy, and hence is more likely to be efficient at driving turbulence, than HII regions expanding into a non-magnetized medium. We find that the magnetic energy added to the cloud by including the effects of MHD is at least as important as the kinetic energy for any type of HII region. More importantly, we find that the kinetic energy lost in going from MHD to hydro is many times less than the magnetic energy gained (§3.3.4). Therefore future studies of HII regions and ionization feedback from star formation should include MHD effects, and since turbulence in MGCs is still poorly understood, the importance of the added magnetic energy from HII regions should be taken into account in efforts that try to understand its origin.

(v) Since the morphology of most MGCs is such that most new born stars are

likely to be near the edge of a cloud, the blister scenario is probably more common than the embedded one. We have performed simulations showing that the blister scenario is in some ways more efficient, in some ways just as efficient, and in other ways less efficient, at affecting the dynamics and evolution of MGCs. Therefore it is important to take into account the blister type scenario in future studies on star formation and turbulence.

Appendix A

Derivation of the Shell Expansion

Rate

Here we will derive the analytic solution of the radius of the shell in the spherical and blister cases. We assume ionization balance, consider the density ρ_{II} constant inside the HII region, and use momentum conservation: $\frac{d\mathcal{P}}{dt} = \mathcal{F}$, where $\mathcal{P}$ is the momentum of the shell and $\mathcal{F}$ is the force applied to it by the pressure inside the HII region. The mass of the shell is $M_{sh} = (4, 2)\pi r^3 \rho_0/3$ since most of the mass inside the Stromgren Sphere is contained in the shell to good approximation, where 4 and 2 are the coefficients for the symmetric and blister cases, respectively. Using ionization balance and Eqn. 1.1 we can write the density inside the HII region:

$$\rho_{II} = \left(\frac{3s\mu_H^2}{4\pi\alpha^{(B)}} \right)^{1/2} r^{-3/2}, \tag{A.1}$$

and hence the pressure inside the HII region:

$$P = (1, 2)\rho_{II}c_{II}^2 = (1, 2)c_{II}^2 \left(\frac{3s\mu_H^2}{4\pi\alpha^{(B)}} \right)^{1/2} r^{-3/2}, \tag{A.2}$$

where the coefficient of 2 for the blister case follows the argument presented in Krumholz & Matzner (2009). Now we use momentum conservation to arrive at the equation of motion:

$$\frac{d\mathcal{P}}{dt} = \frac{d}{dt}\left[(4,2)\pi r^3 \rho_0 \dot{r}/3\right] = \mathcal{F} = P\mathcal{A} = 4\pi r^2 c_{II}^2 \left(\frac{3s\mu_H^2}{4\pi\alpha^{(B)}}\right)^{1/2} r^{-3/2} = 4c_{II}^2 \left(\frac{3s\mu_H^2}{4\pi\alpha^{(B)}}\right)^{1/2} r^{1/2}.$$
(A.3)

$$\implies \frac{(4,2)\rho_0}{3}\left[r^3\ddot{r} + 3r^2\dot{r}^2\right] = 4c_{II}^2 \left(\frac{3s\mu_H^2}{4\pi\alpha^{(B)}}\right)^{1/2} r^{1/2}.$$
(A.4)

This equation can be solved by using a power-law similarity solution.

$$r = r_0 \left(t/t_0\right)^{\eta}.$$
(A.5)

Plugging this into Eqn. A.4, we get

$$\frac{(4,2)\rho_0}{3}\left[\eta(\eta-1)r_0^4\left(\frac{t}{t_0}\right)^{4\eta-2}\frac{1}{t_0^2} + \eta^2 r_0^4\left(\frac{t}{t_0}\right)^{4(\eta-1)}\frac{1}{t_0^2}\right] = 4c_{II}^2\left(\frac{3s\mu_H^2}{4\pi\alpha^{(B)}}\right)^{1/2} r_0^{1/2}\left(\frac{t}{t_0}\right)^{\eta/2}.$$
(A.6)

We need to have the powers of t/t_0 equal on both sides of the equation, so we solve $4\eta - 2 = \eta/2$ for η to find that $\eta = 4/7$. Substituting this back into A.6, we arrive at

$$(4,2)\rho_0\left(\frac{12}{49}\right)\frac{1}{t_0^2} = 4c_{II}^2\left(\frac{3s\mu_H^2}{4\pi\alpha^{(B)}}\right)^{1/2} r_0^{-7/2}.$$
(A.7)

Now we use the fact that $t_s = r_s/c_{II}$ (Eqn. 1.2) to replace c_{II}^2 with r_s^2/t_s^2, and from Eqn. 1.1 we can rewrite ρ_0 as

$$\rho_0 = \left(\frac{3s\mu_H^2}{4\pi\alpha^{(B)}}\right)^{1/2} r_s^{-3/2}.$$
(A.8)

Rearranging everything to solve for r_0, we get

$$r_0 = r_s\left[\frac{49}{(12,6)}\left(\frac{t_0}{t_s}\right)^2\right]^{2/7} = r_s\left[\frac{7}{(\sqrt{12},\sqrt{6})}\left(\frac{t_0}{t_s}\right)\right]^{4/7}.$$
(A.9)

Finally we plug this back into Eqn. A.5 to arrive at our desired solution:

$$r_{sh} = r_s\left(\frac{7t}{\sqrt{12}t_s}\right)^{4/7} (spherical),$$
(A.10)

and

$$r_{sh} = r_s \left(\frac{7t}{\sqrt{6}t_s} \right)^{4/7} (blister). \tag{A.11}$$

Bibliography

Arthur, S., Henney, W., Mellema, G., Colle, F., & Vazquez-Semadeni, E. 2011, mnras, 541

Crutcher, R. M. 1999, ApJ, 178

Gritschneder, M., Naab, T., Walch, S., Burkert, A., & Heitsch, F. 2009, ApJ, 694

Koyama, H. & Inutsuka, S. 2002, ApJ, 564

Krumholz, M. & Matzner, D. 2009, ApJ, 703, 1352

Krumholz, M. & Stone, J. 2007, ApJ, 671

McKee, C. & Ostriker, E. 2007, Annual Reviews of Astronomy and Astrophysics, 45, 565

Osterbrock, D. 1999, Astrophysics of Gaseous Nebulae and Active Galactic Nuclei (Mill Valley: University Science Books)

Spitzer, L. 1978, Physical Processes in the Interstellar Medium (New York: Wiley)

Stone, J., Gardiner, T., Teuben, P., Hawley, J., & Simon, J. 2008, ApJS, 178

Stone, J., Ostriker, E., & Gammie, C. 1998, ApJL, 508